Dynamic integration and segregation of amygdala subregional functional circuits linking to physiological arousal

Yimeng Zeng[1,2#], Fuxiang Tao[1,2,3#], Zaixu Cui[4], Liyun Wu[1,2], Jiahua Xu[1,2,3], Zhi Yang[5], Shaozheng Qin[1,2*]

[1] State Key Laboratory of Cognitive Neuroscience and Learning, Beijing Normal University, Beijing, China;

[2] IDG/McGovern Institute for Brain Research, Beijing Normal University, Beijing, China;

[3] Beijing Key Laboratory of Brain Imaging and Connectomics, Beijing Normal University, Beijing, China;

[4] Department of Psychiatry, Perelman School of Medicine, University of Pennsylvania, Philadelphia, USA;

[5] Shanghai Key Laboratory of Psychotic Disorders, Shanghai Mental Health Center, Shanghai Jiao Tong University School of Medicine, Shanghai, China;

# These authors contributed equally to this work.

Correspondence and requests for materials should be addressed to Y.Z. (yimengzeng@mail.bnu.edu.cn) or S.Q. (szqin@bnu.edu.cn)

Abstract

The dynamical organization of brain networks is essential to support human cognition and emotion for rapid adaption to ever-changing environment. As the core nodes of emotion-related brain circuitry, the basolateral amygdala (BLA) and centromedial amygdala (CMA) are recognized as two major amygdalar nuclei that regulate distinct affective functions and internal autonomic responses via their unique connections with cortical and subcortical structures in rodents. However, little is known how the dynamical organization of emotion-related brain circuitry reflects internal autonomic responses in humans. Using resting-state functional magnetic resonance imaging (fMRI) with concurrent recording of skin conductance, we show robust dynamic integration and segregation states of amygdala subregion-related intrinsic functional networks linked to spontaneous autonomic arousal. To be specific, time-varying connectivity analysis of resting-state fMRI data with K-means clustering approach revealed two distinct states of BLA- and CMA-based connectivity patterns, with a segregation state showing generally stronger BLA- than CMA-based connectivity with cortical regions, and an integration state showing substantial overlapping, in a spatio-temporal manner, between BLA- and CMA-based connectivity networks. Further analysis of skin conductance revealed significantly higher physiological arousal during the integration state than the segregation state, and state-specific BLA- and CMA-based connectivity with distinct subcortical and neocortical targets were predictive of spontaneous fluctuations of skin conductance. Our findings characterize dynamic functional organization of emotion-related amygdala nuclei circuits and networks and its links to spontaneous autonomic arousal in humans.

Keywords: Amygdala, fMRI, dynamic states, arousal, emotion

Introduction

The human brain, as an open and highly sophisticated system, spontaneously abounds with its dynamic nature, allowing a wide range of cognitive and affective functions to be operated in face of ever-changing internal and external demands. Spontaneous activity across large-scale brain networks does not remain constant but undergoes dynamic fluctuations over time (Bassett et al., 2011; Braun et al., 2015), likely at least in part reflecting affective and/or homeostatic states that are closely linked to autonomic and hormonal responses (Dolan, 2002; Calhoun et al., 2014; Deco et al., 2011). Dysregulated intrinsic dynamics of large-scale brain networks critical for emotion and related behaviors has been linked to mood disorders and related to psychiatric conditions (Insel et al., 2004; Sheline et al., 2009; Gentili et al., 2009). The amygdala lies at the core of emotion-related brain networks to broadcast affective state information across widespread brain regions (Murray, 2007; Bickart et al., 2014; Gothard, 2020). However, little is known about the dynamic nature of the amygdala and its functional circuits, and even less is known whether and how their dynamic features are associated with internal autonomic states in humans.

The amygdalar complex encompasses multiple anatomical subregions with distinct connections that support distinct affective functions (LeDoux, 2000; Roy et al., 2009). The basolateral amygdala (BLA) and centromedial amygdala (CMA) are two major groups of amygdalar nuclei that form dedicated networks for distinct functions via their unique pattern of interactions with other cortical and subcortical structures (LeDoux, 2000; LeDoux, 2007). Within the past three decades, there has been great progress in functional neuroimaging techniques that allows researchers to map spontaneous functional coupling of the amygdalar nuclei with large-scale brain networks in vivo in humans (Roy et al., 2009; Etkin et al., 2009; Salzman et al., 2010; Sladky et al., 2015). Seed-based correlation analysis of spontaneous brain activity has been the mainstay of conventional approaches for examining intrinsic functional organization of large-scale brain networks including amygdala-based emotional networks (Raichle et al., 2001; Greicius et al., 2003; Bullmore et al., 2009; Roy et al., 2009). This provides useful information to identify specific target networks with the BLA and CMA, but offers insufficient insight into how these networks dynamically organize over time to regulate the brain's affective functions. Thus, novel

approaches from a dynamic and nonstationary systems perspective are required to mitigate this limitation. Beyond simple scan-length averages (so-called static methods), recent emerging innovative approaches by capturing time-varying properties of connectivity have begun to illustrate the dynamic nature of spontaneous brain activity across large-scale networks in humans (Calhoun et al., 2014). However, the dynamical organization of functional brain networks associated with the amygdalar nuclei still remains open.

There is now increasing evidence converging onto that the dynamic nature of brain functional organization is regulated by the ascending neuromodulatory systems such as locus coeruleus (LC) releasing noradrenaline by acting on widespread brain networks to alter the neuronal excitability and drive the integration of distributed neurons (Aston-Jones & Cohen, 2005). Indeed, the dynamics of network topology has been linked to autonomic arousal levels varying as a function of firing patterns of LC neurons (Aston-Jones & Cohen, 2005; Eldar et al., 2013; Shine et al., 2016). In particular, the amygdalar nuclei including BLA and CMA constitute a large amount of neurotransmitter receptors which could transiently modulate neuronal excitability of the information processing through their projections to specific target circuits and networks (LeDoux, 2007). Critically, one recent study in rodents shows that amygdala neuronal ensembles dynamically encode affective or homeostatic internal states, through two major populations of neurons of the basal nucleus of the amygdala that widely broadcasts internal state information via several output pathways to larger brain networks (Gründemann et al., 2019). Yet, how the dynamical organization of large-scale networks associated with the amygdalar nuclei represent internal autonomic states in humans remains unknown. Our study addresses this critical gap by examining time-varying connectivity patterns of functional circuits associated with the amygdalar nuclei and their links to internal autonomic responses.

Here we addressed the above questions by integrating resting-state functional magnetic resonance imaging (fMRI) with concurrent recording to skin conductance in young healthy adults across two studies to examine how time-varying states of intrinsic functional connectivity of the BLA and CMA reflect autonomic arousal levels. The prior observer-independent cytoarchitectonically determined

probabilistic maps were used to define BLA and CMA (Etkin et al., 2009; Qin et al., 2012). The classical sliding-window approach was implemented to identify time-varying spontaneous functional connectivity of coupling and connected networks of regions (Allen et al., 2014; Fox & Raichle, 2007; Greicius et al., 2003; Sakoğlu et al., 2010), and K-means clustering as one of the popular unsupervised machine-learning algorithms was used to identify dissociable connectivity states. Resting-state fMRI data from a second independent cohort of participants were used for replication analyses to ensure the reproducibility and robustness of the observed dynamic states. We further implemented elastic-net regression to examine whether time-varying connectivity patterns of the amygdalar nuclei are predictive of automimic arousal measured by skin conductance levels. Based on the neurophysiological models of network dynamics and autonomic arousal (Shine et al., 2016; Shine et al., 2018; Young et al., 2017), we predicted that intrinsic connectivity patterns associated with the amygdala nuclei would undergo dissociable time-varying states and such dynamics would predict spontaneous autonomic responses.

Results

Time-varying intrinsic functional connectivity patterns of the BLA and CMA

We first conducted separate seed-based functional connectivity analyses for the BLA and CMA in each hemisphere (see Methods). These analyses revealed a set of widely distributed regions in cortical and subcortical structures whose spontaneous activity are significantly correlated with BLA and CMA seeds, with prominently dissociable patterns in unimodal and polymodal association cortex along with overlapping patterns in limbic structures (**Fig. 1A-B**). Furthermore, we conducted whole-brain 2-by-2 ANOVA with subregions (BLA vs. CMA) and hemispheres (left vs. right) as within-subject factors to identify BLA- and CMA-based target networks (**Fig. S1**). Based on findings from previous studies (Roy et al., 2009; Etkin et al., 2009; Qin et al., 2012), we selected five target networks of our major interest in a set of widely distributed network, including 1) limbic and paralimbic structures, 2) uni- and polymodal association cortex, 3) subcortical structures, 4) Cerebellum and 5) prefrontal cortex (see Methods). Thereafter, we examined conventional scan-length averages of intrinsic functional

connectivity associated with the BLA and CMA. This analysis revealed that spontaneous activity of the BLA seed showed stronger coupling with activity in a set of widely distributed cortical, paralimbic, and limbic structures, whereas spontaneous activity of the CMA showed stronger coupling with activity in subcortical regions as well as the cerebellum (**Fig. 1C**). This dissociation is in line with findings from previous studies on static intrinsic functional connectivity (Roy et al., 2009; Qin et al., 2012).

Next, we implemented a sliding window approach in conjunction with K-means clustering methods to examine time-varying intrinsic functional connectivity properties of five target networks associated with the BLA and CMA (**Fig. 1D**). The window length was set to 30 TR and movement step was set to 1 TR. The optimal number of clusters were determined by Silhouette coefficient (Rousseeuw, 1987) and CalinskiHarabasz criterion (Caliński and Harabasz, 1974), in which higher value indicates larger cohesion and less dispersity. This analysis revealed highest scores under both Silhouett coefficient and CalinskiHarabasz criterion scores at cluster numbers set to 2 (**Fig. 1E**). To ensure the stability of time-varying connectivity and the reliability of clustering, we additionally computed the two metrics using a set of window lengths (α) and steps (β) varying from 30 to 50 TRs and 1 to 3 TRs respectively (**Fig. 1F, S2**). These results revealed consistent patterns of outcomes, with two clearly dissociable states of time-varying BLA and CMA connectivity patterns (**Fig. 2A**). Critically, these two states were reproducible in an independent cohort 2 with 21 participants (**Fig. S3**).

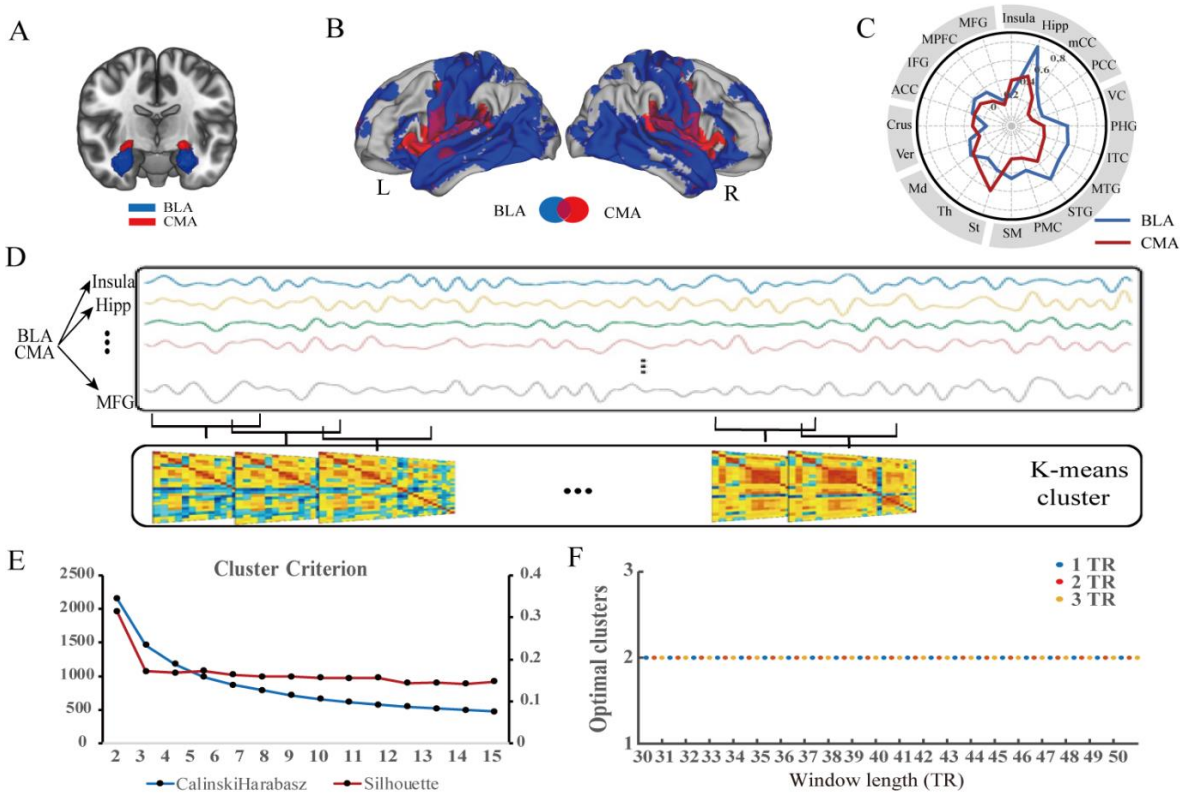

Figure 1. An overview of time-varying functional connectivity of emotion-related brain networks by sliding window and K-means clustering. (**A**) A coronal view of the BLA (blue) and CMA (red) seeds. (**B**) Lateral views of significant clusters derived from BLA- and CMA-based intrinsic functional connectivity, and the overlapping areas are colored in pink. (**C**) Polar plots show BLA- and CMA-based intrinsic functional connectivity strength with target regions in uni- and polymodal association cortex, para-limbic and subcortical structures, and prefrontal cortex. (**D**) An illustration of K-means cluster analysis for Cohort 1. Connectivity matrice between BLA/CMA seed regions and 20 target regions were computed in each window. (**E**) Line curves depict the CalinskiHarabasz and Silhouette criteria as a function of cluster number K. (**F**) Different combination of window length and step were used to quantify the most optimal parameters. The vertical coordinate represents silhouette score and the horizontal axis represents window length varying from 30TR to 50TR. Different color dots represent different steps varying from 1TR to 3TR. Notes: L, left; R, right; BLA, basolateral amygdala; CMA, centromedial amygdala.

Integration and segregation states linking to distinct spatiotemporal BLA and CMA connectivity patterns

To further examine the differences in two distinct states (denoted as State 1 and State 2), we compared the intrinsic functional strength of BLA and CMA-target networks within and between State 1 and State 2across participants (**Fig. 2B).** Firstly, separate independent t tests for averaged functional connectivity (Fisher-z transformed) revealed significantly higher BLA-based connectivity strength than that of CMA, in both State 1 [$t_{(4308)}$ = 33.34, two tailed p < 0.001] and State 2[$t_{(3922)}$ = 39.16, two tailed p < 0.001]. These results are consistent with previous studies as a generalized pattern for adults (Qin et al., 2012) and validate our clustering result. More interestingly, we found both BLA-associated and CMA-associated connectivity in State 1 are significantly higher than that in State 2 (separate independent t tests, BLA: $t_{(8230)}$ = 78.34, two tailed p < 0.001; CMA: $t_{(8230)}$ = 106.34, two tailed p < 0.001). Additionally, edge by edge comparisons exhibited similar patterns mentioned above (**Table. S1, S2).** These results indicate distinct difference between the two states, as the one showing higher amygdalar subregional connectivity with associated target regions than the other. Furthermore, we calculated intra-network similarity between BLA and CMA-target networks for the two states, measured by their averaged Pearson correlation values (Fisher's r-to-z transformed). (**Fig. 2C**). This analysis revealed significantly higher similarity between BLA and CMA target networks in State 1(r = 0.59), when compared to that in State 2 (r = 0.35, two sample t-test, $t_{(8230)}$ = 18.60, two tailed p < 0.001). Additionally, we conducted a windowed time lagged cross-correlation (WTLCC) analysis (Boker et al., 2002; Cryer et al., 2008;) to examine the temporal relationship between BLA and CMA-target networks in the two distinct states (**Fig. 2D**). To do this, concatenated time series during two states were binned, creating sequence of epochs for cross correlation computations at different time lags (see Methods). We observed that the highest WTLCC in each epoch more frequently emerged around lag zero in State 1 compared

with that in State 2. To validate this, we averaged WTLCC across all epochs for State 1 and State 2 separately (**Fig. 2E**), and separate independent t tests revealed that State 1 showed significant higher averaged WTLCC than that in State 2 at lag of zero (separate independent t tests, $ts_{(203)} > 2.92$, two tailed $p < 0.05$, FDR corrected), suggesting higher functional coupling between BLA- and CMA-target networks in State 1 than that in State 2. Notably, all the results are reproducible in independent cohort 2 (**Fig. S3**), indicating a robust characterization for these two states across cohorts. Interestingly, we calculated averaged occupancy of two states at each window for the two cohorts and found distinct dynamics regarding to the emergence and occupancy rate between them during evolution (**Fig. S4**), suggesting a highly individual-specific manner for these two distinct states.

Overall, by implementing sliding-window approach with K-means clustering method, we found a clear dissociation of spatio-temporal evolution patterns for BLA- and CMA-based intrinsic connectivity within two states. Based on the highly integrative nature for State 1 and segregated behavior for State 2, we denote State 1 as integration state and State 2 as segregation state for the rest of the study.

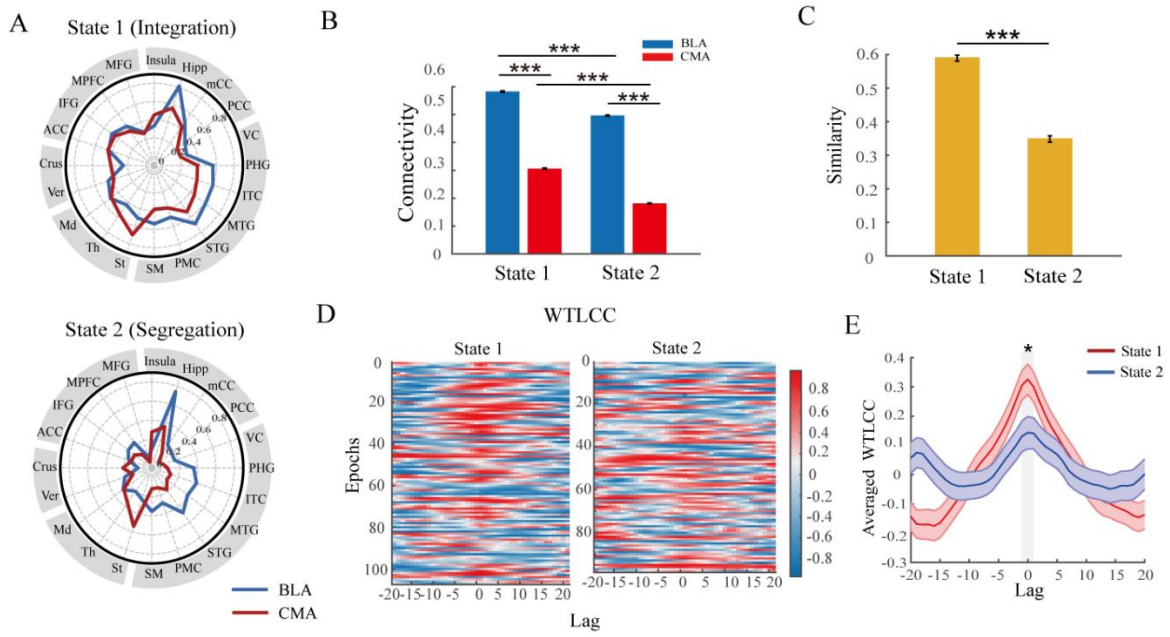

Figure 2. Time-varying integration and segregation states related to distinct spatial-temporal patterns for BLA and CMA connectivity networks. (**A**) Polar plots depict two distinct states, with generally stronger connectivity strength of both BLA (blue) and CMA (red) with target ROIs for integration state, while significantly weaker yet dissociable connectivity between BLA and CMA seeds. (**B**) Bar graphs (top) shows significant difference in connectivity strength between BLA- (blue) and CMA-based target regions (red) for each state. (**C**) Bar graphs (bottom) shows averaged correlation of BLA- and CMA-target connectivity networks within integration and segregation state, respectively. (**D**) Heat map depicts windowed time-lagged cross-correlation (WTLCC) for State 1 and State 2. The x-axes represent cross correlation between BLA- and CMA-target networks under different time lag (offset). The y-axes represent the number of bins (epochs) under different conditions. Color represent correlation value for each lag, each epoch. (**E**) The curves depict averaged WTLCC for State 1 (red) and State 2 (blue) separately and the shaded area depicts standard error of mean for each WTLCC. Ranges of lags showing significant higher averaged WTLCC of State 1 than State 2 are marked by gray area (FDR corrected). Notes: *$P < 0.05$; **$P < 0.01$; ***$P < 0.001$.

Time-varying states of BLA and CMA connectivity predict spontaneous autonomic arousal

After detecting distinct dynamic states, we further examined whether they can be robustly linked to spontaneous autonomic arousal. Based on the fact that results for dynamic state clustering are robust across Cohort 1 and 2 (**Fig. 2A, S3**), here we implemented Cohort 2 (N=21) with concurrent recording of spontaneous skin conductance levels (SCL) and treat them as a function of time-varying integration and segregation state evolution (**Fig. 3A**). Skin conductance data was first down-sampled, detrended and bandpass-filtered. Then SCL data was normalized within each participant to facilitate the comparable and interpretable purposes (Boucsein,1992; Patterson et al., 2002; Fan et a., 2012), with 5 out of 21 subjects in Cohort 2 excluded from further analysis due to poor SCL quality (see Methods). Similar with previous studies (Tambini et al., 2017), the SCL levels were window-wise averaged to match the length of each dynamic state. Independent t test for window-wise SCL data for windows within two dynamic states revealed significantly higher SCL in the integration than segregation state [$t_{(3214)} = 2.58$, two tailed $p < 0.01$] (**Fig. 3B**). In addition, we also computed the averaged window-wise SCL for each state per participant. Paired t test for this individual level comparison revealed a similar tendency, with higher SCL in integration than segregation state [$t_{(15)} = 1.94$, $p = 0.035$ one tailed].

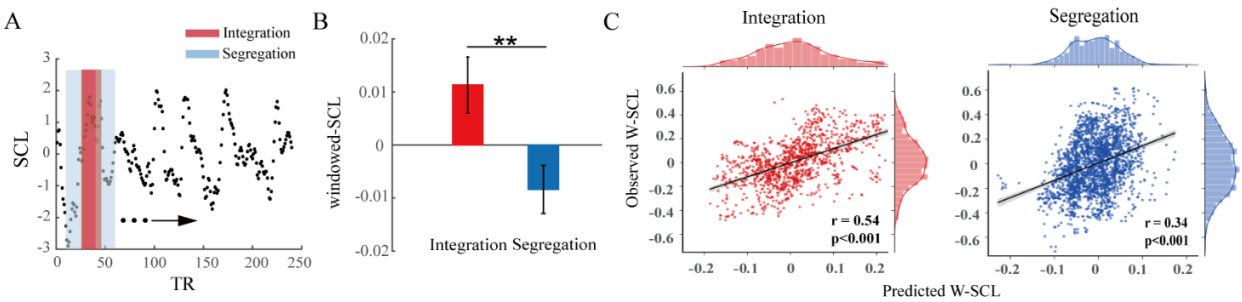

Figure 3. Time-varying integration and segregation states link to spontaneous skin conductance levels (SCLs). (**A**) An example of preprocessed SCL data in each window as a function of integration and segregation states. Data points within each window were averaged to quantify an overall SCL level of each dynamic state. (**B**) Bar graphs depict window-wise averaged SCL during integration and segregation states on the group level. (**C**) Scatter plots show the significant correlations between the predicted and actual values using the elastic-net regression in the integration and segregation states respectively. Notes: * P < 0.05; ** P

< 0.01; *** P < 0.001.

To make a further step, we implemented elastic-net regression model to examine whether dynamic states, featured by their time-varying functional networks of BLA- and CMA-seed, can robustly predict window-wise SCL fluctuations (see Methods). First, total 40 dynamic connections were extracted as a feature vector (i.e. 1×40 vector) and corresponding windowed SCL extracted as response variable for each temporal window. Then two elastic-net models were implemented for integration and segregation state separately, with 10-fold cross validation to determine hyperparameters (α, λ) (**Fig. S5**). These analyses revealed significant correlations between the predicted and actually observed data of SCLs for both integration (r = 0.54, permutated p < 0.001) and segregation states (r = 0.34, permutated p < 0.001) (**Fig. 3C**), indicating a link between SCL fluctuations and dynamic states of BLA-/CMA-based target connectivity networks. Further, to compare the difference of prediction accuracy between two models, we implemented bootstrapping method (see Methods), generating two distributions of the bootstrapped prediction accuracy. Separate independent t tests for these two distributions revealed a significantly higher prediction accuracy for SCLs in the integration than segregation states ($t_{(1998)}$ = 78.48,two tailed p < 0.001). Together, these results indicate that time-varying BLA and CMA connectivity patterns are predictive of concurrent SCL fluctuations, with higher SCL levels during integration than segregation states.

Distinct time-varying BLA and CMA target networks predict autonomic arousal

We further investigated how specific configurations of BLA and CMA target networks in integration and segregation states contribute to predicting spontaneous SCL fluctuations. By extracting contribution weights (absolute coefficients) derived from elastic-net regression

models of the integration and segregation states (**Fig. S6**), we observed that in integration state, more target network links is considered effective for predicting SCLs (only 7 of total 40 features assigned zero weight), as compared to those in segregation state (12 of total 40 features assigned zero weight) (**Fig. 4A, 4C)**. Moreover, total contribution weights of integration state are also higher than that of segregation state. These results are consistent with their distinct predicted accuracy and suggest tenser functional link between SCLs and integration state (**Fig. 3C**). We further calculated the relative ratio of total contribution weights between BLA- and CMA-target links and robustly observed an BLA-leading contribution phenomenon in integration state while a CMA-dominated pattern in segregation state (**Fig.S7**). Subsequently, spatial distribution for the top 25% contributing links was visualized for integration and segregation state (**Fig. 4B, 4D)** and we found most contributed links are specified by distinct dynamic states. For the integration state, these links involved middle cingulate cortex, hippocampus and middle temporal gyrus while sensory motor cortex, anterior and posterior cingulate cortex were unique for segregation state. Together, these results indicate dissociable BLA and CMA target network configurations in the integration and segregation states to predict spontaneous SCL levels.

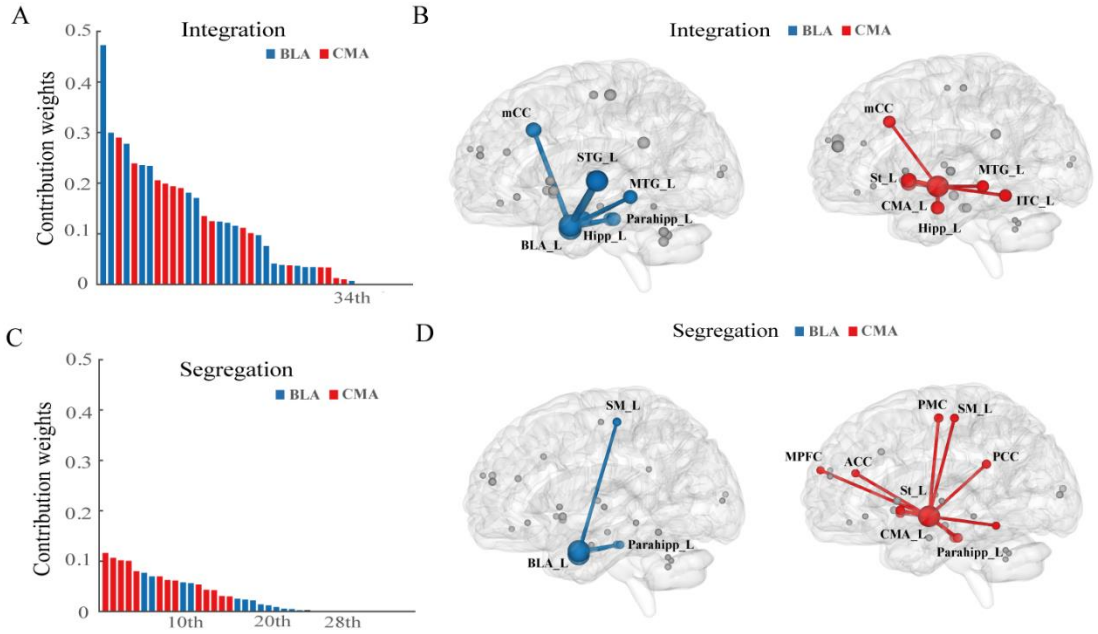

Figure 4. Weights and spatial distributions of BLA and CMA-based target network configurations linking to spontaneous SCL fluctuations. (A, C) Bar graphs depict BLA and CMA target network connections derived from the elastic-net model, ranked by their absolute weights, for integration (top) and segregation (bottom) states. (**B**, **D**) Top 25% links of BLA (blue) and CMA (red) target networks during the integration and segregation are superimposed onto the glass brain in a sagittal view separately, with links in the left hemisphere for visualization purpose only. Size of nodes and corresponding links represent the relative contribution weights of BLA- and CMA-target links derived from elastic-net model.

Discussion

In this study, we investigated the dynamical organization of intrinsic functional connectivity networks associated with the amygdala nuclei and its contributions to autonomic arousal in humans. By leveraging machine learning and clustering approaches, we identified two distinct states of time-varying intrinsic connectivity networks: an integration state exhibits generally stronger connectivity but substantial integrative patterns between BLA- and CMA-based target networks, whereas a segregation state exhibits relatively weaker yet dissociable BLA- than CMA-based connectivity with cortical regions. There is a clear dissociation of spatio-temporal evolution patterns for BLA- and CMA-based intrinsic connectivity within the integration and segregation states. Critically, such time-varying dissociable states of BLA- and CMA-based target networks are linked to spontaneous SCLs – a measure

of autonomic arousal, with integration state exhibiting significantly higher SCL as compared to the segregation state. Such time-varying integration and segregation states with distinct BLA- and CMA-based network configurations contribute to predicting spontaneous fluctuations of SCLs.

We found two distinct states of time-varying intrinsic connectivity patterns for BLA and CMA target networks by implementing sliding-window and K-mean clustering methods. Specifically, the integration state showed generally stronger connectivity with all of target ROIs and substantially overlapping between BLA and CMA target networks, as compared with the segregation state. Unlike the integration state, however, the segregation state showed clearly functional dissociation between BLA and CMA target networks: the BLA showed stronger connectivity with widespread regions in uni- and poly-association cortical areas, (para)limbic structures and prefrontal cortex, while the CMA showed stronger connectivity with the striatum. This segregation pattern partially is somewhat in line with previous findings on functional segregation of BLA and CMA target networks using the conventional scan-length averaging (static-like) approaches (Roy et al., 2009; Etkin et al., 2009; Qin et al., 2012). Building on the neuroanatomical models in rodents with the amygdalar nuclei via unique connections to form specific dedicated circuits in support of distinct affective functions (LeDoux, 2000; LeDoux, 2007), our observed time-varying integration and segregation states provide prominent evidence to highlight a dynamic functional reorganization of BLA- and CMA target networks over time in humans. For the integration state, our observed tightly coupling patterns between BLA and CMA target networks are not reported by the conventional scan-length averaging functional connectivity approaches. Notably, such dynamic integration and segregation pattern is reproducible by another independent cohort of participants, suggesting the reproducibility and robustness of our current findings. Together, these two dynamic states provide novel evidence to suggest that BLA and CMA intrinsic functional circuits do not remain constant, rather undergo spontaneously fluctuated over time. This extends previous findings on intrinsic functional organization of the amygdalar nuclei derived from conventional (static-like) approaches and animal models.

A second major finding of our study is that time-varying integration and segregation states were

predictive of spontaneous fluctuations of SCLs. In particular, we found significantly stronger SCL in time windows during the integration state than the segregation state. Numerous psychophysiological studies have demonstrated a link of skin conductance levels with internal autonomic or physiological arousal (Critchley et al., 2010; Boucsein, 2012). Thus, it is conceivable that our observed higher skin conductance level during the integration state might reflect higher autonomic or physiological arousal. From a systems level, converging evidence from human functional neuroimaging and animal studies suggests an increase in BOLD-fMRI signals and neuronal excitability in large-scale neural networks closely linked to elevation of autonomic arousal due to the activation of (non)adrenergic systems (Chang et al., 2009; Phelps et al., 2005; Hermans et al., 2011; Kim et al., 2017). For instances, animal studies have demonstrated that LC releasing norepinephrine (Aston-Jones & Cohen, 2005) acts on corresponding receptors in widely distributed brain regions especially the amygdala and related networks, thereby prompting rapid increases in neuronal excitability and functional coupling among these disparate regions (Arnsten, 1998). This notion is highly relevant to with our observed significantly stronger connectivity among BLA and CMA target networks in the integration state, as well as one recent finding on the association of salience-network cohesion with autonomic arousal (Young et al., 2017).

Moreover, our observed substantial overlapping between BLA and CMA target networks in the integration state may reflect increased functional coordination of large-scale neural networks accompanying with high levels of autonomic arousal measured by pupillometry data in humans (Murphy et al., 2011; Shine et al., 2016). Animal model have also shown that high levels of arousal during acute stress can trigger a widespread cascade of neurochemical changes that rapidly prompt neuronal excitability of large-scale brain networks into a tonically high mode (Joëls & Baram, 2009; Stujenske & Likhtik, 2017). Thus, it is possible that there are multiple neuromodulatory systems contributing to our observed stronger yet overlapping pattern between BLA and CMA target networks in the integration state. In other words, the integration state may result from endogenous autonomic and hormonal stimulations promoting the excitability of neuronal ensembles in the amygdalar nuclei and related functional circuits, thereby promoting the flexibility of the brain's internal affective or

homeostatic states to meet ever-changing environmental needs. Indeed, evidence from recent studies have suggested that integrated states may enable faster and more effective performance on a cognitive task, most likely through ascending neuromodulatory systems to regulate the transition between multiple modes of brain function (Shine et al., 2016; Shine et al., 2018).

A third important finding of our study is that distinct features (or connections) from time-varying states of BLA and CMA target networks contribute to predicting spontaneous autonomic arousal as evidenced by SCLs. Specifically, a balanced contribution of BLA- and CMA- target networks for predicting SCLs may suggest an integrative nature relating to high autonomic arousal during the integration state, when compared with a dominated contribution of CMA-associated networks during the segregation state. Such divergence between two dynamic states may exhibit distinct arousing modes, with one owning highly integrative phenomenon between BLA and CMA-based target networks and the other exhibiting CMA-dominated pattern between them. Such highly dynamical phenomenon of amygdala-based intrinsic functional networks is somehow in line with newly emerging evidence from recent animal research, which demonstrates that amygdala ensembles can dynamically represent internal affective or homeostatic states (Janak et al., 2015; Beyeler et al.,2018; Zhang et al., 2018). Specifically, the dynamic assembly of two major populations of neurons in the BLA plays a role in regulating animal's internal autonomic or physiological states through several output pathways to larger brain networks (Salzman et al., 2010; Zhang et al., 2018; Grundemann et al., 2019).

Furthermore, the divergence between these two states were further supported by their distinct spatial distributions among most effective links mainly at (para)limbic structures, including the anterior,medial and posterior portions of the cingulate cortex, the hippocampus, and unimodal association cortex such as sensory motor cortex and medial temporal gyrus. These dissociable patterns may reflect an integrative role in converging information from multiple brain systems that are modulated by the amygdalar nuclei. Besides, many studies in humans and animal models have shown that functional coordination among the amygdala, insula, cingulate cortex, and sensorimotor areas contributes to information integration closely related to affective, homeostatic and cognitive states (Craig, 2002;

Critchley, 2004; Devinsky et al., 1995; Pollatos et al., 2007), and with increased activation and connectivity within the salience network in response to stress (Hermans et al., 2011; McMenamin et al., 2014). This somehow resembles findings from previous studies showing that patients with seizures can alter consciousness, affective states and expression, as well as autonomic responses, through its abundant projections into sensory-motor cortex and polymodal association areas (Devinsky et al., 1995). In addition, the amygdala is recognized to play a critical role in affective information processing likely through its functional coupling with regions in polymodal association areas and the prefrontal cortex in emotion perception, appraisal and regulation (Lim et al., 2009). Thus, it is likely to speculate that our observed BLA and CMA target networks in the integration and segregation states may reflect internal physiological responses with different levels of arousal involved in a variety of cognitive and affective functions.

The dynamical (re)organization of large-scale brain networks holds the promise to enable the flexibility of brain functioning and rapid adaptation in face of ever-changing environmental demands (Braun et al., 2015; Deco et al.,2010; McMenamin et al., 2014). To our knowledge, no studies to date have directly investigated the dynamical organization of amygdala subregional functional circuits and networks. Our findings thus extend the existing knowledge on functional organization of emotion-related brain circuitry which is theorized to play a critical role in regulating one's internal autonomic (and more broadly homeostatic) states. This line of research has its potential to extend into investigating function and dysfunction of emotion-related brain circuitry in affective disorders including anxiety and depression. The mainstay of previous studies using the conventional approaches have demonstrated emotion-related brain dysconnectivity in patients with affective disorders , with hyper- and/or hypo-connectivity patterns in limbic, paralimbic and prefrontal systems critical for vigilance, rapid detection and memories for threatening stimuli, emotion regulation and expression (Bishop, 2007; Clark, & Beck, 2010; Sturm et al., 2007). Thus, it would be highly relevant to investigate how dysregulated brain dynamics as well as functional circuits linked to the amygdalar nuclei in particular underlie the core symptoms of affective disorders. Understanding the dynamical organization of emotion-related brain circuitry represents an important step toward developing brain-inspired biomarkers of affective and

psychosomatic disorders on a circuit-level (Insel et al., 2010; Deisseroth, 2014). Future studies are required to delineate how the dynamical organization of the amygdalar nuclei with broader networks regulates internal affective or autonomic responses in both healthy and psychiatric conditions.

In conclusion, our study demonstrates dynamic integration and segregation of the emotion-related brain networks that are linked to different internal autonomic states. Our findings provide important implications into understanding the neurobiological mechanisms of how the dynamical organization of emotion-related brain networks regulates internal physiological states, and eventually inform dysregulated brain dynamics in affective disorders and psychopathology.

Materials and Methods

Participants

This study included a total of 63 young healthy participants from two independent cohorts. The first cohort consisted of 42 young healthy participants (mean age ± SD: 22.62 ± 0.99 years ranged from 21 to 24, 27 females) after dropping out invalid participants because of excessive head motion (Cohort 1). A second independent cohort of 21 adults matched in age and sex (mean age ± SD: 22.71 ± 1.68 years ranged from 20 to 25, 11 female) was recruited to undergo fMRI with the concurrent recording of skin conductance (Cohort 2). All of the participants reported no history of any neurological or psychiatric disorders, and no current use of any medication or recreational drugs. The experiment and procedures were approved by the Institutional Review Board for Human Subjects at Beijing Normal University in accordance with the standards of the Declaration of Helsinki. Written, informed consent was obtained from all participants before the experiment.

Imaging acquisition

For Cohort 1, brain images were acquired from a Siemens 3T scanner (Siemens Magnetom Prisma syngo MR D13D, Erlangen, Germany) with a 64-channel phased-array head coil in Peking University. Participants were instructed to keep their eyes open and remain still for a period of 8-min resting-state fMRI scan. T2-weighted images were recorded using an echo-planar imaging (EPI) sequence, with 177 volumes (axial slices, 33; slice thickness, 3.5 mm; volume repetition time, TR, 2000 ms; echo time, TE, 30 ms; flip angle, 90; voxel size, 3.5 x 3.5 x 3.5 mm; field of view, FOV, 224 x 224 mm). High-resolution anatomical T1-weighted images were collected using three-dimensional sagittal T1-weighted magnetization-prepared rapid gradient echo (MPRAGE) sequence (192 slices; TR, 2530 ms; TE, 2.98 ms; slice thickness, 1 mm; flip angle, 7°; voxel size, 0.5 x 0.5 x 1.0 mm; FOV, 256 x 256 mm).

For Cohort 2, whole-brain imaging data were collected on a 3T Siemens Prisma MRI system in Peking

University. Functional images were collected using a multi-band echo-planar imaging (mb-EPI) sequence (slices, 64; slice thickness, 2 mm; TR, 2000 ms; TE, 30 ms; flip angle, 90°; multiband accelerate factor, 2; voxel size, 2.0 × 2.0 × 2.0 mm; FOV, 224 × 224 mm). Structural images were acquired through three-dimensional sagittal T1-weighted magnetization-prepared rapid gradient echo (MPRAGE) sequence (192 slices; TR, 2530 ms; TE, 2.98 ms; slice thickness, 1 mm; voxel size, 1.0 × 1.0 × 1.0 mm, interpolated to 0.5 × 0.5 × 1.0 mm; flip angle, 7°; inversion time, 1100 ms; FOV, 256 × 256 mm). Field map images were acquired with grey field mapping sequence (64 slices; TR, 635 ms; TE1, 4.92 ms; TE2, 7.38 ms; slice thickness, 2 mm; voxel size, 2.0 × 2.0 × 2.0 mm; flip angle, 60°; FOV, 224 × 224 mm).

Skin conductance (SC) recording

SC data were recorded simultaneously with fMRI scanning using a MRI-compatible Biopac MP 150 System (Biopac, Inc., Goleta, CA). Two Ag/AgCl electrodes filled with isotonic electrolyte medium were attached to the center phalanges of the index and middle fingers of the left hand. The gain set to 5, the low pass filter set to 1.0 Hz to reduce scanner-induced noise, and the high pass filters set to DC. Data were acquired at 1000 samples per second.

Skin conductance level (SCL) analysis

The SCR waveform was first downsampled by averaging data points within each 2 s window to match repetition time (TR) of MR scanning during imaging data acquisition. The SCR waveform was then detrended to remove slow linear drift of the SCLs. Next, the detrended SCR data was bandpass-filtered within the frequency range of 0.008 - 0.1 Hz in accordance with intrinsic functional connectivity analysis of resting-state fMRI data. Finally, SCL data was normalized within each participant to facilitate the comparable and interpretable purposes (Braithwaite et al., 2013; Boucsein et al., 2012). The preprocessed SCL time series was further averaged within the same sliding window to match the dynamic state (window length: 40 TRs)

Imaging preprocessing

Functional imaging preprocessing was performed using tools from Statistical Parametric Mapping SPM12 (http://www.fil.ion.ucl.ac.uk/spm). The first five volumes were discarded for signal equilibrium, and the last two volumes were also discarded in case participants' impatience. Images using multi-band EPI sequence were additionally corrected for distortions related to magnetic field inhomogeneity in combination with field map images. After that, functional images were corrected for slice acquisition timing. Subsequently, functional images were co-registered to each participant's gray matter image segmented from corresponding high-resolution T1-weighted image, then spatially normalized into a common stereotactic Montreal Neurological Institute (MNI) space and resampled into 2 mm. Finally, images were smoothed by an isotropic three-dimensional Gaussian kernel with 6 mm full-width at half-maximum.

Regions of interest (ROIs) definition

Four ROIs encompassing the BLA and CMA for each hemisphere were created separately using cytoarchitectonically defined probabilistic maps of the amygdala. Maximum probability maps were used to create nonoverlapping amygdala subregions using the Anatomy Toolbox (Eickhoff SB, et al. 2005). Voxels were included in the maximum probability maps only if the probability of their assignment to the BLA or CMA was higher than any other nearby structures with greater than 40% likelihood. Each voxel was exclusively assigned to only one region. Overlapping voxels were assigned to the region that had the greatest probability, resulting in two nonoverlapping ROIs representing CMA and BLA subregions for each hemisphere. Based on the previous study (Qin et al., 2012), we selected the same five target networks of interest – subcortical structures including striatum, thalamus and midbrain; crus and vermis/declive regions of the cerebellum; uni- and polymodal association cortex including visual cortex (VC), parahippocampal gyrus (PHG), inferior temporal cortex (ITC), middle (MTG) and superior temporal gyrus (STG), premotor cortex (PMC) and sensorimotor cortex (SM);

limbic and paralimbic structures including hippocampus (Hipp), insula (Ins), middle (mCC) and posterior (PCC) portions of cingulate cortex; and prefrontal cortex including anterior cingulate cortex (ACC), middle (MFG) and inferior frontal gyrus (IFG), and medial prefrontal cortex (MPFC).

Functional connectivity analysis

Time series of each seed (averaging across all voxels within ROI) were filtered with a bandpass temporal filter (0.008 to 0.10 Hz) and extracted. Six motion parameters, cerebrospinal fluid and white matter of each participant that account for potential physiological noise and movement-related artifacts were regarded as covariates of no interest. Subsequently, the resultant time series were demeaned. For each participant, two separate functional connectivity analyses were performed for both BLA and CMA for each hemisphere separately. The contrast parameter images for each of the four seed ROIs from the individual level analyses were submitted to a second-level group analysis by treating participants as a random variable in a 2-by-2 ANOVA with amygdala subregions (BLA vs. CMA) and hemispheres (left vs. right) as within-subject factors. Significant clusters were estimated with a height threshold of $p < 0.05$(FDR corrected) and an extent threshold of $p < 0.1$(voxel size: 30).

Similar to previous studies in adults, target ROIs of each seed were determined from the group-level analyses for significant BLA- and CMA-based connectivity networks in combination with conventional AAL template. Meanwhile, lateral BLA and CMA seed regions were combined separately for following analysis. Finally, both times series of each seed and associated target ROIs were extracted by the same procedure mentioned above and Pearson's correlation, representing the strength of functional connectivity of each seed with corresponding target masks, were computed between amygdala subregion-seeded time series and target time series.

Dynamic functional connectivity analysis

Dynamic functional connectivity was assessed using a widely used sliding-window approach (Sakoğlu et al., 2010; Bassett et al., 2011; Allen 2014; Shine et al., 2016) in MATLAB R2015b (MathWorks, Natick, USA). The entire temporal time series were divided into a series of windows with a specific window length ($\alpha = 40$ TR) and step ($\beta = 1$ TR). The total quantity of windows was defined by a parameter W,

$$\mathrm{W} = \lfloor (\mathrm{T} - \alpha)/\beta \rfloor + 1$$

where T is a total number of time points. Initial point S for each window i was defined as:

$$S_i = 1 + (i - 1)\beta\,, i = 1, \ldots, W$$

while endpoint E was defined as:

$$E_i = (i - 1)\beta + \alpha\,, i = 1, \ldots, W$$

First, Pearson's correlation coefficients between BLA and CMA seed and associated target ROIs were calculated within each time window. Each participant's BLA- and CMA-seed functional connectivity within each time window were transformed into one-dimensional vectors. Next, K-means clustering of windowed correlation matrices was implemented to quantify different states of dynamics of BLA- and CMA-based functional connectivity. The algorithm was repeated with 1000 random iterations to exclude the sensitivity of K-means to initial conditions.

A paramount step of clustering analysis is determining the optimal parameter set $(\mathrm{K}, \alpha, \beta)$. Various parameter sets were attempted to fulfill this goal ($K = 2 - 10$, sliding window length $\alpha = 30 - 50$ TRs, step $\beta = 1.0 - 3.0$ TRs). The optimal parameter set (2, 40, 1) were obtained after evaluation of silhouette coefficient (P Rousseeuw, 1987) and CalinskiHarabasz criterion (T Caliński & J Harabasz, 1974), in which the former evaluation considered cohesion and dispersity while the later criterion evaluated covariance between inter-group and intra-group.

Windowed time-lagged cross-correlation analysis for BLA and CMA-networks of dynamic states

We implemented time lagged cross correlation (TLCC) for the integration state and segregation states separately. We first sequentially concatenated all of the time series of target ROIs belonging to the different states across participants. We then averaged time series for the BLA and CMA target ROIs during different states separately. To calculate cross-correlation of the BLA and CMA-network evolution, we binned each time series according to the total length of time series of two cohorts (Cohort 1: 8221 TRs in total; Cohort 2: 4221 TRs in total). The time-lag range (offset) was set within -20 to 20 for each window or epoch (bin), resulting in the numbers of epochs (Cohort 1: 98 epochs for the integration state, 107 epochs for the segregation state; Cohort 2: 41 epochs for the integration state, 64 epochs for the segregation state:). After that, cross-correlation value for each offset in each bin was Fisher-z transformed for further statistical analyses (**Fig. 2D**).

Machine learning-based prediction analysis

Elastic-net regression models was implemented to identify most contributed connections of the BLA and CMA target networks critical to predict spontaneous SCL fluctuations (Z. Cui et al., 2018). The Statistics and Machine Learning Toolbox in MATLAB 2015a (MathWorks, Natick, USA) was used to performance the elastic net regression (Boyd S., 2010). Elastic-net model earns the benefits of excluding little-contributed variables while reducing overfitting problem by implementing L1 and L2-regularization in the model (controlled by parameter α and λ separately). For training procedure, windowed dynamic connections between BLA and CMA and their associated networks (total 40 connections) were extracted as feature vector of integration and segregation separately and their corresponding window-SCL were treated as response. Then to determine the optimal parameter set (α, λ) for the elastic-net model we applied a grid search, with alpha chosen from 20 values in the range of [0.05, 1.0] and lambda chosen from 100 values generated from a default lambda sequence. Then model was applied 10-fold cross-validation to examine performance of elastic net regression at different

parameter settings (**Fig. S5**). Finally, (α, λ) with minimum cross-validation error plus one standard deviation was selected for later analysis (Tsankov et al., 2015). The Statistics and Machine Learning Toolbox in MATLAB 2015a (MathWorks, Natick, USA) was used to perform the elastic net regression (Boyd S., 2010) and related figures. The permutation tests were applied to determine whether the obtained final correlation for integration-SCL and segregation-SCL links were significantly better than expected by chance (Dosenbach et al., 2010). Specifically, the above prediction procedure was repeated for 5000 times and only temporal SCL of training data were shuffled within each resampling. The *p* value of the mean correlation *r* was calculated by dividing the number of permutations that showed a higher value than the actual value for the real sample by the total number of permutations.

Bootstrapping for comparison of correlation between integration and segregation state

A bootstrapping method was implemented to examine the difference of correlation between window-wise SCLs and associated two dynamic states. Specifically, we conducted repeated resampling from total SCL-state pairs of integration state and integration state separately. Then we employed elastic-net model with the same hyperparameters settings used in **Fig. 3C**, to estimate the correlation of resampled SCL- integration (integration) state pairs separately. We thus created simulated distribution of Pearson's correlation for integration (integration) states and associated SCLs. Then two sample t test was employed to compare the difference of these two distributions (Fisher-z transformed). The resample times was set to 1000 and the population size for each resample was set to 750 (Efron et al., 1994).

References

[1]. Adolphs R, Tranel D, Damasio H, Damasio A. 1994. Impaired recognition of emotion in facial expressions following bilateral damage to the human amygdala. *Nature* **372**:669-72.

[2]. Allen, E. A., Damaraju, E., Plis, S. M., Erhardt, E. B., Eichele, T., & Calhoun, V. D. 2014. Tracking

whole-brain connectivity dynamics in the resting state. *Cerebral cortex* **24**:663-676.

[3]. Amunts, K., Kedo, O., Kindler, M., Pieperhoff, P., Mohlberg, H., Shah, N. J., ... & Zilles, K. 2005. Cytoarchitectonic mapping of the human amygdala, hippocampal region and entorhinal cortex: intersubject variability and probability maps. *Anatomy and embryology* **210**:343-352.

[4]. Arnsten, A. F. (1998). The biology of being frazzled. *Science* **280**:1711-1712.

[5]. Aston-Jones, G., & Cohen, J. D. 2005. An integrative theory of locus coeruleus-norepinephrine function: adaptive gain and optimal performance. *Annu. Rev. Neurosci* **28**:403-450.

[6]. Baczkowski, B. M., Johnstone, T., Walter, H., Erk, S., & Veer, I. M. 2017. Sliding-window analysis tracks fluctuations in amygdala functional connectivity associated with physiological arousal and vigilance during fear conditioning. *Neuroimage* **153**:168-178.

[7]. Bassett, D. S., Wymbs, N. F., Porter, M. A., Mucha, P. J., Carlson, J. M., & Grafton, S. T. 2011. Dynamic reconfiguration of human brain networks during learning. *Proceedings of the National Academy of Sciences* **108**:7641-7646.

[8]. Beyeler, A. et al. 2016. Divergent routing of positive and negative information from the amygdala during memory retrieval. *Neuron* **90**:348–361.

[9]. Beyeler, A. et al. 2018. Organization of valence-encoding and projection-defined neurons in the basolateral amygdala. *Cell Rep* **22**:905–918.

[10]. Bickart, K.C., B.C. Dickerson, and L. Feldman Barrett. 2014. The amygdala as a hub in brain networks that support social life. *Neuropsychologia* **63**:235-248.

[11]. Bishop, S. J. 2007. Neurocognitive mechanisms of anxiety: an integrative account. *Trends in cognitive sciences* **11**:307-316.

[12]. Boker S.M., Rotondo J.L., Xu M, King K. 2002. Windowed cross-correlation and peak picking for the analysis of variability in the association between behavioral time series. *Psychological Methods*. **7**:338-355.

[13]. Boucsein, W. (2012). *Electrodermal activity*. Springer Science & Business Media.

[14]. Braithwaite, J. J., Watson, D. G., Jones, R., & Rowe, M. 2013. A guide for analysing electrodermal activity (EDA) & skin conductance responses (SCRs) for psychological experiments. *Psychophysiology* **49**: 1017-1034.

[15]. Braun, U., Schäfer, A., Walter, H., Erk, S., Romanczuk-Seiferth, N., Haddad, L., ... & Meyer-

Lindenberg, A. 2015. Dynamic reconfiguration of frontal brain networks during executive cognition in humans. *Proceedings of the National Academy of Sciences* **112**:11678-11683.

[16]. Bressler, S. L., & Menon, V. 2010. Large-scale brain networks in cognition: emerging methods and principles. *Trends in cognitive sciences* **14**:277-290.

[17]. Boyd, S. 2010. Distributed Optimization and Statistical Learning via the Alternating Direction Method of Multipliers. *Foundations and Trends in Machine Learning*. **3**:1–122.

[18]. Cahill, L., & McGaugh, J. L. 1998. Mechanisms of emotional arousal and lasting declarative memory. *Trends in neurosciences* **21**:294-299.

[19]. Caliński T, Harabasz J. A dendrite method for cluster analysis. 1974. *Communications in Statistics-theory and Methods* **3**:1-27.

[20]. Campolongo, P., Roozendaal, B., Trezza, V., Hauer, D., Schelling, G., McGaugh, J. L., & Cuomo, V. 2009. Endocannabinoids in the rat basolateral amygdala enhance memory consolidation and enable glucocorticoid modulation of memory. *Proceedings of the National Academy of Sciences* **106**:4888-4893.

[21]. Chang, C., J.P. Cunningham, and G.H. Glover. 2009. Influence of heart rate on the BOLD signal: The cardiac response function. *NeuroImage* **44**:857-869.

[22]. Christianson, S. A. 2014. *The handbook of emotion and memory: Research and theory*. Psychology Press.

[23]. Clark, D. A., & Beck, A. T. 2010. Cognitive theory and therapy of anxiety and depression: Convergence with neurobiological findings. *Trends in cognitive sciences* **14**:418-424.

[24]. Colibazzi, & T. 2014. Journal watch review of research domain criteria (rdoc): toward a new classification framework for research on mental disorders. *Journal of the American Psychoanalytic Association* **62**:709-710.

[25]. Craig, A. D. 2002. How do you feel? Interoception: the sense of the physiological condition of the body. *Nature reviews neuroscience* **3**:655.

[26]. Critchley, H. D. 2004. The human cortex responds to an interoceptive challenge. *Proceedings of the National Academy of Sciences* **101**:6333-6334.

[27]. Critchley, H.D. 2010. Electrodermal Responses: What Happens in the Brain. *The Neuroscientist* **8**:132-144.

[28]. Cryer J. D., Chan K-S., 2008. *Time Series Analysis with Applications in R*. New York Springer.

[29]. Davis, M. 1997. Neurobiology of fear responses: the role of the amygdala. *The Journal of neuropsychiatry and clinical neurosciences* **9**:382-402.

[30]. de Gee, J. W., Colizoli, O., Kloosterman, N. A., Knapen, T., Nieuwenhuis, S., & Donner, T. H. 2017. Dynamic modulation of decision biases by brainstem arousal systems. *Elife* **6**:e23232.

[31]. Deco, G., Jirsa, V. & McIntosh, A. 2011. Emerging concepts for the dynamical organization of resting-state activity in the brain. *Nat Rev Neurosci* **12**:43–56.

[32]. Deco G, Corbetta M. 2011. The dynamical balance of the brain at rest. *Neuroscientist* **17**:107-23.

[33]. Deco, G.; Jirsa, V.; Friston, K.J. 2012. *The dynamical structural basis of brain activity. In Principles of Brain Dynamics: Global State Interactions*. Cambridge, MA: MIT Press.

[34]. Deisseroth, & Karl. 2014. Circuit dynamics of adaptive and maladaptive behaviour. *Nature* **505**:309-317.

[35]. Devinsky, O., Morrell, M. J., & Vogt, B. A. 1995. Contributions of anterior cingulate cortex to behaviour. *Brain* **118**:279-306.

[36]. DiCiccio, T.J. and Efron B. 1996. Bootstrap confidence intervals. *Statistical Science* **11**:189-228.

[37]. Dolan, R. J., & Vuilleumier, P. 2003. Amygdala automaticity in emotional processing. *Annals of the New York Academy of Sciences* **985**:348-355.

[38]. Dosenbach N U F, Nardos B, Cohen A L, et al. 2010. Prediction of individual brain maturity using fMRI. *Science* **329**:1358-1361.

[39]. Dosenbach, N. U., Nardos, B., Cohen, A. L., Fair, D. A., Power, J. D., Church, J. A., ... & Barnes, K. A. 2010. Prediction of individual brain maturity using fMRI. *Science* **329**:1358-1361.

[40]. Drucker H, Burges C J C, Kaufman L, et al. 1997. Support vector regression machines. *Advances in neural information processing systems* **9**:155-161.

[41]. Efron, Bradley, and Robert Tibshirani. 1994. *An Introduction to the Bootstrap*. New York: Chapman & Hall, Print.

[42]. Eickhoff, S. B., Stephan, K. E., Mohlberg, H., Grefkes, C., Fink, G. R., Amunts, K., & Zilles, K. 2005. A new SPM toolbox for combining probabilistic cytoarchitectonic maps and functional imaging data. *Neuroimage* **25**:1325-1335.

[43]. Eldar, E., Cohen, J. D., & Niv, Y. 2013. The effects of neural gain on attention and learning. *Nature neuroscience* **16**:1146.

[44]. Etkin, A., Prater, K. E., Schatzberg, A. F., Menon, V., & Greicius, M. D. 2009. Disrupted amygdalar subregion functional connectivity and evidence of a compensatory network in generalized anxiety disorder. *Archives of general psychiatry* **66**:1361-1372.

[45]. Fox, M. D., & Raichle, M. E. 2007. Spontaneous fluctuations in brain activity observed with functional magnetic resonance imaging. *Nature reviews neuroscience* **8**:700.

[46]. Gentili, C., et al. 2009. Beyond amygdala: Default Mode Network activity differs between patients with Social Phobia and healthy controls. *Brain Research Bulletin* **79**:409-413.

[47]. Gothard, K.M. 2020. Multidimensional processing in the amygdala. *Nature Reviews Neuroscience* **21**:565-575.

[48]. Greicius, M. D., Krasnow, B., Reiss, A. L., & Menon, V. 2003. Functional connectivity in the resting brain: a network analysis of the default mode hypothesis. *Proceedings of the National Academy of Sciences* **100**:253-258.

[49]. Gründemann, J., et al.2019. Amygdala ensembles encode behavioral states. *Science* **364**: eaav8736.

[50]. Hermans, E. J., Van Marle, H. J., Ossewaarde, L., Henckens, M. J., Qin, S., Van Kesteren, M. T., ... & Fernández, G. 2011. Stress-related noradrenergic activity prompts large-scale neural network reconfiguration. *Science* **334**:1151-1153.

[51]. Insel, T.R. and R.D. Fernald. 2004. How the Brain Processes Social Information: Searching for the Social Brain. *Annual Review of Neuroscience* **27**:697-722.

[52]. Janak, P. H. & Tye, K. M. 2015. From circuits to behaviour in the amygdala. *Nature* **517**:284–292.

[53]. Joëls, M., & Baram, T. Z. 2009. The neuro-symphony of stress. *Nature reviews neuroscience* **10**:459.

[54]. Kim, J., et al. 2017. Basolateral to Central Amygdala Neural Circuits for Appetitive Behaviors. *Neuron* **93**:1464-1479.

[55]. Kim, E. J., Kong, M. S., Park, S. G., Mizumori, S. J., Cho, J., & Kim, J. J. 2018. Dynamic coding of predatory information between the prelimbic cortex and lateral amygdala in foraging rats. *Science advances* **4**:eaar7328.

[56]. Krishnamurthy, K., Nassar, M. R., Sarode, S., & Gold, J. I. 2017. Arousal-related adjustments of perceptual biases optimize perception in dynamic environments. *Nature human behavior* **1**:0107.

[57]. LeDoux, J. 2007. The amygdala. *Current biology* **17**:R868-R874.

[58]. LeDoux, J. E. 2000. Emotion circuits in the brain. *Annual review of neuroscience* **23**:155-184.

[59]. Lim, S. L., Padmala, S., & Pessoa, L. 2009. Segregating the significant from the mundane on a moment-to-moment basis via direct and indirect amygdala contributions. *Proceedings of the National Academy of Sciences* **106**:16841-16846.

[60]. McGaugh, J. L. 1992. *The Handbook of Emotion and Memory*. Research and Theory.

[61]. McGaugh, J. L. 2000. Memory--a century of consolidation. *Science* **287**:248-251.

[62]. McGaugh, J. L. 2002. Memory consolidation and the amygdala: a systems perspective. *Trends in neurosciences* **25**:456-461.

[63]. McGaugh, J. L., Cahill, L., & Roozendaal, B. 1996. Involvement of the amygdala in memory storage: interaction with other brain systems. *Proceedings of the National Academy of Sciences* **93**:13508-13514.

[64]. McMenamin, B. W., Langeslag, S. J., Sirbu, M., Padmala, S., & Pessoa, L. 2014. Network organization unfolds over time during periods of anxious anticipation. *Journal of Neuroscience* **34**:11261-11273.

[65]. Mehrabian, A., & Russell, J. A. 1974. *An approach to environmental psychology*. the MIT Press.

[66]. Menon, V., & Uddin, L. Q. 2010. Saliency, switching, attention and control: a network model of insula function. *Brain Structure and Function* **214**:655-667.

[67]. Murphy, P.R., et al. 2011. Pupillometry and P3 index the locus coeruleus–noradrenergic arousal function in humans. *Psychophysiology* **48**:1532-1543.

[68]. Murray, E.A. 2007. The amygdala, reward and emotion. *Trends in Cognitive Sciences* **11**:489-497.

[69]. Nichols, T., & Hayasaka, S. 2003. Controlling the familywise error rate in functional neuroimaging: a comparative review. *Statistical methods in medical research* **12**:419-446.

[70]. Panksepp, J. B., & Lahvis, G. P. 2011. Rodent empathy and affective neuroscience. *Neuroscience & Biobehavioral Reviews* **35**:1864-1875.

[71]. Pessoa, L., & Adolphs, R. 2010. Emotion processing and the amygdala: from a'low road'to'many roads' of evaluating biological significance. *Nature reviews neuroscience* **11**:773.

[72]. Phelps, E.A. and J.E. LeDoux. 2005. Contributions of the Amygdala to Emotion Processing: From Animal Models to Human Behavior. *Neuron* **48**:175-187.

[73]. Pollatos, O., Gramann, K., & Schandry, R. 2007. Neural systems connecting interoceptive awareness and feelings. *Human brain mapping* **28**:9-18.

[74]. Popescu, A. T., Popa, D., & Paré, D. 2009. Coherent gamma oscillations couple the amygdala and striatum during learning. *Nature neuroscience* **12**:801.

[75]. Qin, S., Young, C. B., Duan, X., Chen, T., Supekar, K., & Menon, V. 2014. Amygdala subregional structure and intrinsic functional connectivity predicts individual differences in anxiety during early childhood. *Biological psychiatry* **75**:892-900.

[76]. Qin, S., Young, C. B., Supekar, K., Uddin, L. Q., & Menon, V. 2012. Immature integration and segregation of emotion-related brain circuitry in young children. *Proceedings of the National Academy of Sciences* **109**:7941-7946.

[77]. Rousseeuw P J. 1987. Silhouettes: a graphical aid to the interpretation and validation of cluster analysis. *Journal of computational and applied mathematics* **20**:53-65.

[78]. Roy, A. K., Shehzad, Z., Margulies, D. S., Kelly, A. C., Uddin, L. Q., Gotimer, K., ... & Milham, M. P. 2009. Functional connectivity of the human amygdala using resting state fMRI. *Neuroimage* **45**:614-626.

[79]. Sakoğlu, Ü., Pearlson, G. D., Kiehl, K. A., Wang, Y. M., Michael, A. M., & Calhoun, V. D. 2010. A method for evaluating dynamic functional network connectivity and task-modulation: application to schizophrenia. *Magnetic Resonance Materials in Physics, Biology and Medicine* **23**:351-366.

[80]. Sladky, R., et al. 2015. Disrupted Effective Connectivity Between the Amygdala and Orbitofrontal Cortex in Social Anxiety Disorder During Emotion Discrimination Revealed by Dynamic Causal Modeling for fMRI. *Cerebral Cortex* **25**:895-903.

[81]. Salzman, C. D., & Fusi, S. 2010. Emotion, cognition, and mental state representation in amygdala and prefrontal cortex. *Annual review of neuroscience* **33**:173-202.

[82]. Sheline, Y.I., et al. 2009. The default mode network and self-referential processes in depression. *Proceedings of the National Academy of Sciences* **106**:1942.

[83]. Shine, J. M., Aburn, M. J., Michael, B. , & Poldrack, R. A. 2018. The modulation of neural gain facilitates a transition between functional segregation and integration in the brain. *eLife* **7**: e31130.

[84]. Shine, J. M., Bissett, P. G., Bell, P. T., Koyejo, O., Balsters, J. H., Gorgolewski, K. J., ... & Poldrack, R. A. 2016. The dynamics of functional brain networks: integrated network states during cognitive task performance. *Neuron* **92**:544-554.

[85]. Stujenske, J. M., & Likhtik, E. 2017. Fear from the bottom up. *Nature Neuroscience* **20**:765-767.

[86]. Sturm, V., et al. 2003. The nucleus accumbens: a target for deep brain stimulation in obsessive–compulsive- and anxiety-disorders. *Journal of Chemical Neuroanatomy* **26**:293-299.

[87]. A. M. Tsankov, V. Akopian, R. Pop, S. Chetty, C. A. Gifford, L. Daheron, et al., 2015. A qPCR ScoreCard quantifies the differentiation potential of human pluripotent stem cells. *Nature Biotechnology* **33**: 1182-1192.

[88]. Valentino, R. J., & Van Bockstaele, E. 2008. Convergent regulation of locus coeruleus activity as an adaptive response to stress. *European journal of pharmacology* **583**:194-203.

[89]. Xia M, Wang J, He Y. 2013. BrainNet Viewer: A Network Visualization Tool for Human Brain Connectomics. *PLoS ONE* **8**: e68910.

[90]. Young, C. B., Raz, G., Everaerd, D., Beckmann, C. F., Tendolkar, I., Hendler, T., ... & Hermans, E. J. 2017. Dynamic shifts in large-scale brain network balance as a function of arousal. *Journal of Neuroscience* **37**:281-290.

[91]. Yu, K., Ahrens, S., Zhang, X., Schiff, H., Ramakrishnan, C., Fenno, L., ... & He, M. 2017. The central amygdala controls learning in the lateral amygdala. *Nature neuroscience* **20**:1680-1685.

[92]. Z. Cui, M. Su, L. Li, H. Shu and G. Gong. 2018. Individualized Prediction of Reading Comprehension Ability Using Gray Matter Volume. Cerebral Cortex 28:1656-1672.

[93]. Zhang, X. and B. Li. 2018. Population coding of valence in the basolateral amygdala. *Nature Communications* **9**:5195.

Acknowledgements: This work was supported by the National Natural Science Foundation of China (31522028, 81571056, 2014NT15), the Open Research Fund of the State Key Laboratory of Cognitive Neuroscience and Learning (CNLZD1503), the Fundamental Research Funds for the Central Universities and the BNU Interdisciplinary Research Foundation for the First-Year Doctoral Candidates (BNUXKJC1910).

Supplement Materials

Table S1. Brain regions that show significant differences in functional connectivity between integration and segregation state, computed separately in CMA- and BLA-seed target networks

Brain regions		BLA-network		CMA-network	
		State 1 versus State 2			
		T values	*p* values	T values	*p* values
Limbic and paralimbic structures	Insula	40.15	***	33.24	***
	Hippocampus	29.38	***	43.63	***
	mCC	53.81	***	67.39	***
	PCC	27.55	***	39.59	***
Uni- and polymodal association cortex	VC	20.44	***	30.53	***
	Parahippocampal gyrus	40.78	***	57.48	***
	ITC	38.22	***	55.14	***
	MTG	48.20	***	70.33	***
	STG	48.76	***	71.73	***
	PMC	37.75	***	49.64	***
	SM	34.95	***	44.34	***
Subcortical structures	Striatum	51.77	***	41.04	***
	Thalamus	38.46	***	47.79	***
	Midbrain	41.30	***	44.77	***
Cerebellum	Vermis/declive	40.60	***	49.09	***
	Crus	33.53	***	30.67	***
Prefrontal cortex	ACC	48.94	***	60.53	***
	IFG	48.53	***	60.12	***
	MPFC	38.52	***	55.42	***
	MFG	43.42	***	51.10	***

Notes: All *p* values were corrected by FDR. *P < 0.05; **P < 0.01; ***P < 0.001; n.s., no significance. mCC,

middle portions of cingulate cortex; PCC, posterior portions of cingulate cortex; VC, visual cortex; ITC, inferior temporal cortex; MTG, middle temporal gyrus; STG, superior temporal gyrus; PMC, premotor cortex; SM, sensorimotor cortex; ACC, anterior cingulate cortex; IFG, inferior frontal gyrus; MPFC, medial prefrontal cortex; MFG, middle frontal gyrus.

Table S2. Brain regions that show significant difference in functional connectivity difference (BLA versus CMA) between integration versus segregation

Brain regions		State 1		State 2	
		BLA versus CMA			
		T values	*p* values	T values	*p* values
Limbic and paralimbic structures	Insula	-35.50	***	-34.58	***
	Hippocampus	92.28	***	94.77	***
	mCC	22.45	***	23.25	***
	PCC	31.37	***	34.32	***
Uni- and polymodal association cortex	VC	18.25	***	23.45	***
	Parahippocampal gyrus	47.41	***	55.10	***
	ITC	52.64	***	54.89	***
	MTG	47.46	***	53.46	***
	STG	50.85	***	60.14	***
	PMC	28.10	***	30.23	***
	SM	37.77	***	40.31	***
Subcortical structures	Stratum	-66.30	***	-62.83	***
	Thalamus	-37.55	***	-27.71	***
	Midbrain	5.27	***	2.81	**
Cerebellum	Vermis/declive	17.09	***	16.77	***
	Crus	-36.83	***	-31.29	***
Prefrontal cortex	ACC	-1.83	n.s.	6.53	***
	IFG	12.70	***	16.96	***
	MPFC	19.73	***	30.57	***
	MFG	6.35	***	11.13	***

Notes: All notes and abbreviations are the same as that in Table S1.

Table S3. Coefficients of brain regions in predicting SCLs derived from ElasticNet model (integration state)

Brain regions		BLA	CMA
		weight	weight
Limbic and paralimbic structures	Insula	0.096	-0.032
	Hippocampus	-0.298	0.237
	mCC	0.276	0.198
	PCC	0.180	-0.134
	VC	0.033	0
	Parahippocampal gyus	0.234	-0.110
Uni- and polymodal association cortex	ITC	0	0.204
	MTG	0.233	0.192
	STG	-0.471	-0.100
	PMC	-0.075	0
	SM	-0.169	0.036
Subcortical structures	Stratum	0.122	-0.289
	Thalamus	-0.006	0.032
	Midbrain	-0.037	-0.123
Cerebellum	Vermis/declive	-0.114	0
	Crus	-0.120	-0.009
Prefrontal cortex	ACC	-0.040	0
	IFG	-0.033	-0.011
	MPFC	0	0
	MFG	0.035	-0.189

Notes: CMA, centromedian amygdala; BLA, basolateral amygdala. [a], this weight is the contribution of the functional connectivity between BLA and CMA. Other notes and abbreviations are the same as that in Table S1.

Table S4. Coefficients of brain regions in predicting SCLs derived from ElasticNet model (segregation state)

Brain regions		BLA	CMA
		weight	weight
Limbic and paralimbic structures	Insula	0.011	-0.052
	Hippocampus	0	0.029
	mCC	-0.003	-0.029
	PCC	0	-0.100
	VC	-0.001	0.041
	Parahippocampal gyrus	-0.068	-0.115
Uni- and polymodal association cortex	ITC	0.024	0.060
	MTG	0	0
	STG	0.004	0
	PMC	0	0.105
	SM	0.076	-0.079
Subcortical structures	Striatum	-0.055	0.099
	Thalamus	-0.013	0
	Midbrain	-0.008	-0.042
Cerebellum	Vermis/declive	0	0
	Crus	0.023	0
Prefrontal cortex	ACC	0.021	0.068
	IFG	0	0
	MPFC	1.82E-05	0.061
	MFG	0.056	0.001

Notes: All notes and abbreviations are the same as that in Table S3.

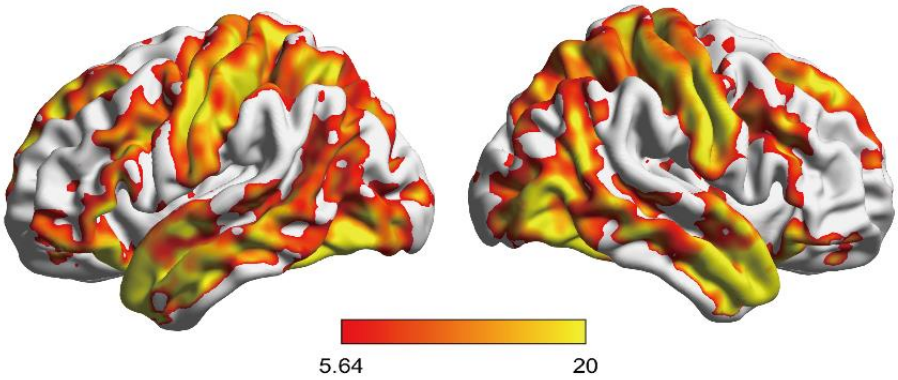

Fig S1. Anova result on cohort 1. Brain regions exhibiting significant interactions, with subregions (BLA vs. CMA) and hemisphere (left vs. right) as within-subject factors.

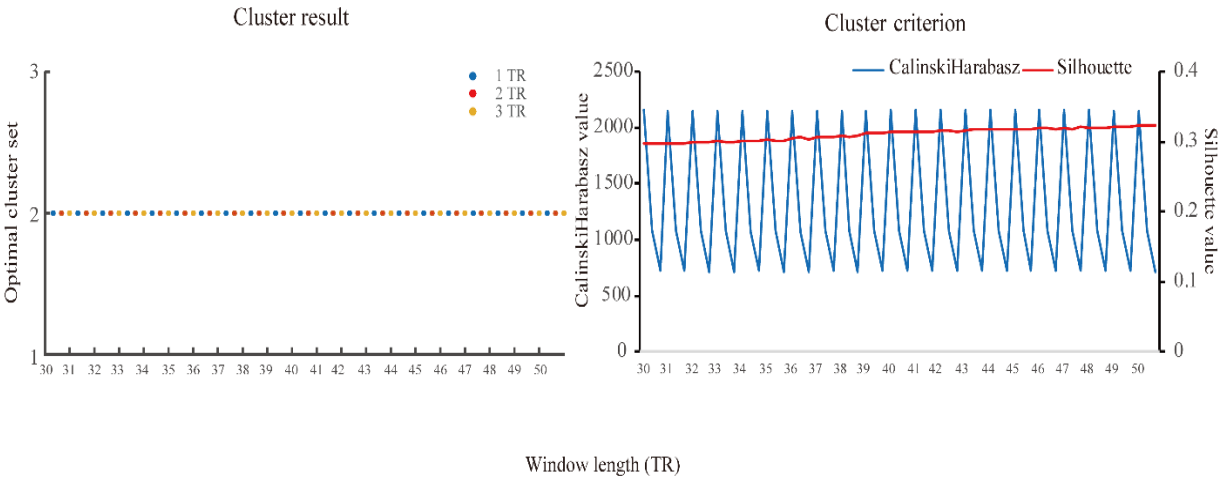

Fig S2. Parameters selection. Different combination of window length and step were used to quantify the most optimal parameters. The vertical coordinate represents silhouette score and the horizontal axis represents window length varying from 30TRs to 50TRs. Different color dots represent different steps varying from 1TR to 3TRs.

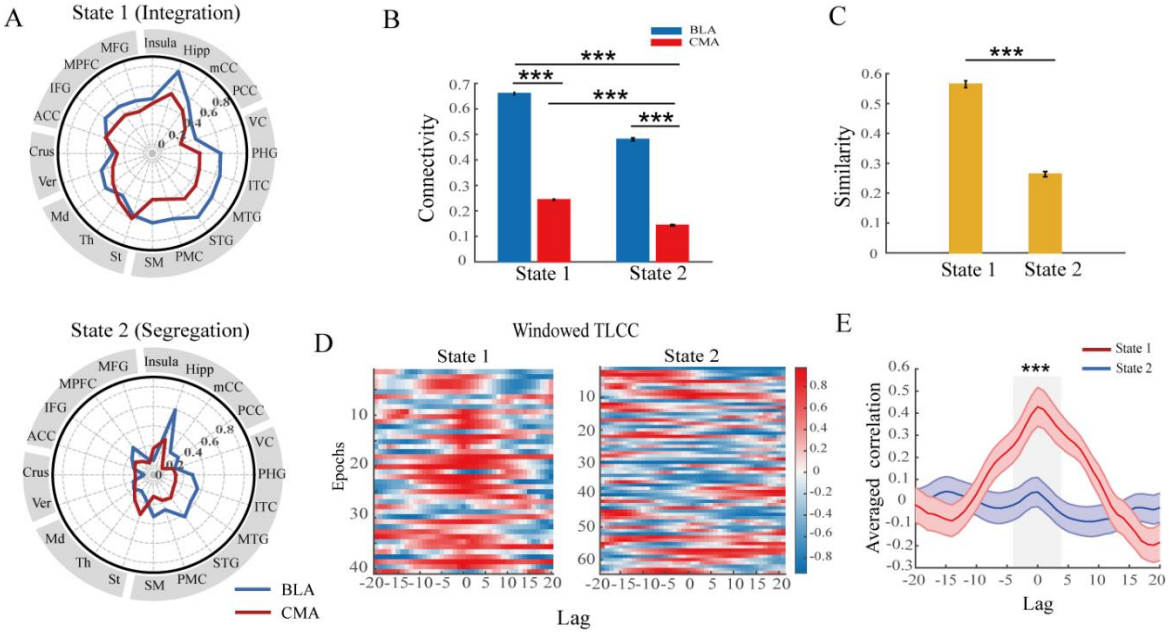

Figure S3. Replication results in independent Cohort 2. (**A**) Polar plots depict two distinct states similar with those in Cohort 1. (**B**) Bar graphs (top) shows significant difference in connectivity strength between BLA- (blue) and CMA-based target regions (red) for each state. (**C**) Bar graphs (bottom) shows averaged correlation of BLA- and CMA-target connectivity networks within integration and segregation state, respectively. (**D**) Heat map depicts windowed time-lagged cross-correlation (WTLCC) for State 1 and State 2. The x-axes represent cross correlation between BLA- and CMA-target networks under different time lag (offset). The y-axes represent the number of bins (epochs) under different conditions. Color represent correlation value for each lag, each epoch. (**E**) The curves depict averaged WTLCC for State 1 (red) and State 2 (blue) separately and the shaded area depicts standard error of mean for each WTLCC. Ranges of lags showing significant higher averaged WTLCC of State 1 than State 2 are marked by gray area (FDR corrected). Notes: *$P < 0.05$; **$P < 0.01$; ***$P < 0.001$.

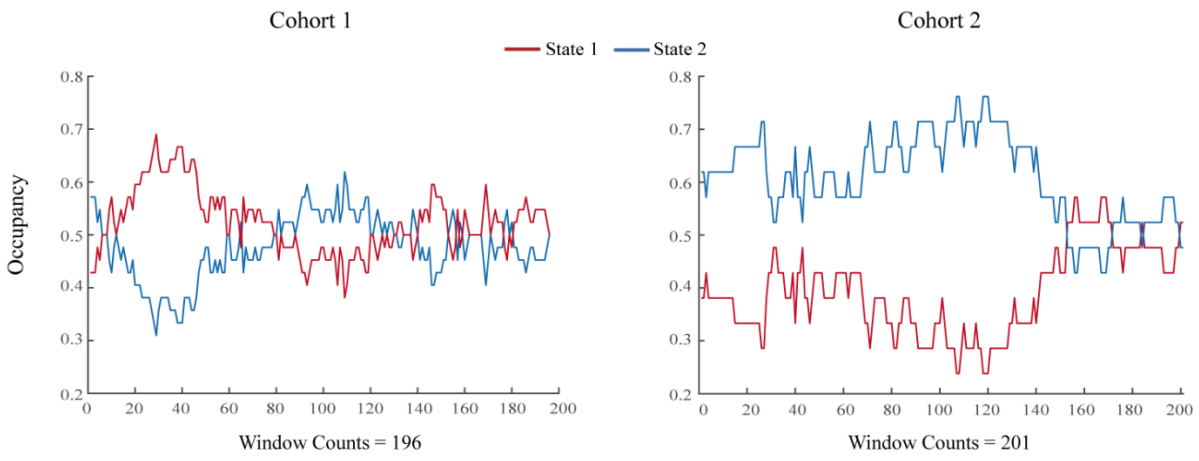

Fig S4. The post hoc occupancy of integration and segregation in two cohorts. The occupancy of State 1 (red) and State 2 (blue) across all the participants are calculated by post hoc assignment after K-means clustering and plotted at each window. The x-axes represent total window counts for cohort 1 and cohort 2, the y-axes represents occupancy.

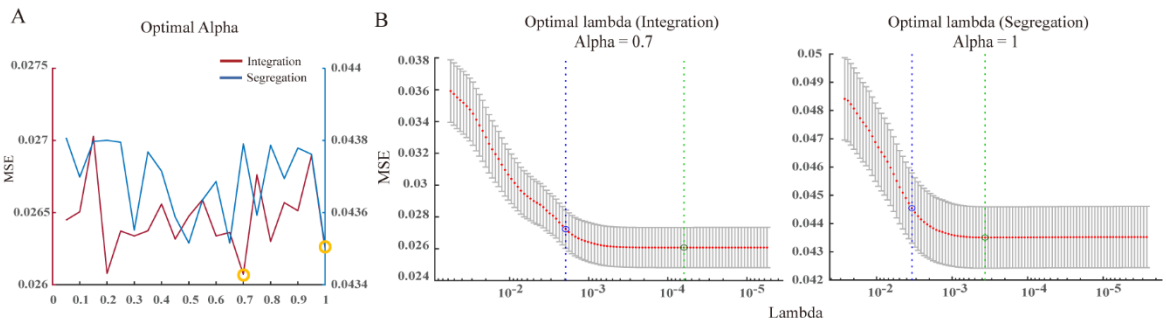

Figure S5. Parameter selection procedure for Alpha and Lambda in elastic-net model.

(A) For each α, we calculated MSE under different λ and depicted the minimum MSE at each α value in integration (red line) and segregation (blue line) separately. X axis represent different α while y axis represents values of MSE for integration (red, left) and segregation (blue, right) separately. Yellow circles represent chosen α values for two states separately which has the minimum MSE from all possible parameter settings. (B) Plots depict MSE under different λ values for integration (left) and segregation (right), after determining the optimal α values. Error bars represents the standard of the MSE computed by 10-fold cross-validation. The green circles indicate the Lambda with one minimum MSE. The blue circles indicate the largest lambda such that the MSE is within on standard error of the

minimum MSE.

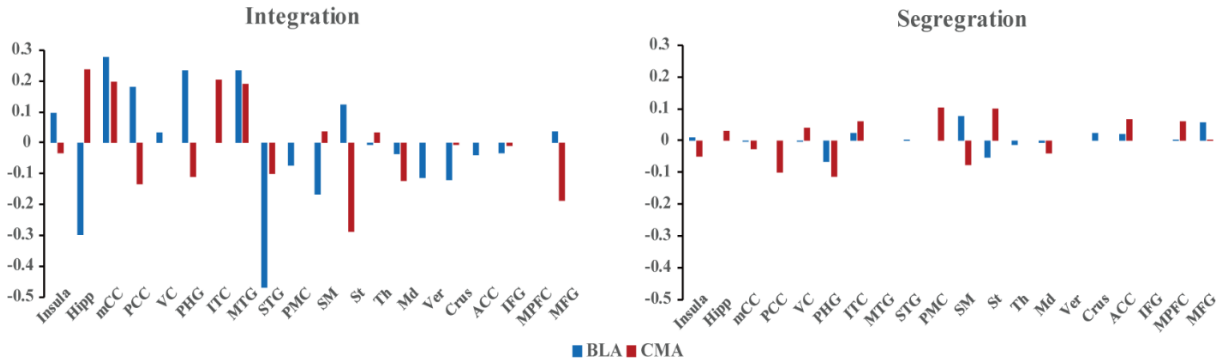

Figure S6. Contribution of each feature and dominated features in integration and segregation states. Bar graphs depict absolute contribution weights for BLA-target ROIs (blue) and CMA-target ROIs (red) derived from elastic-net regression model in integration (top) and segregation (bottom) states separately.

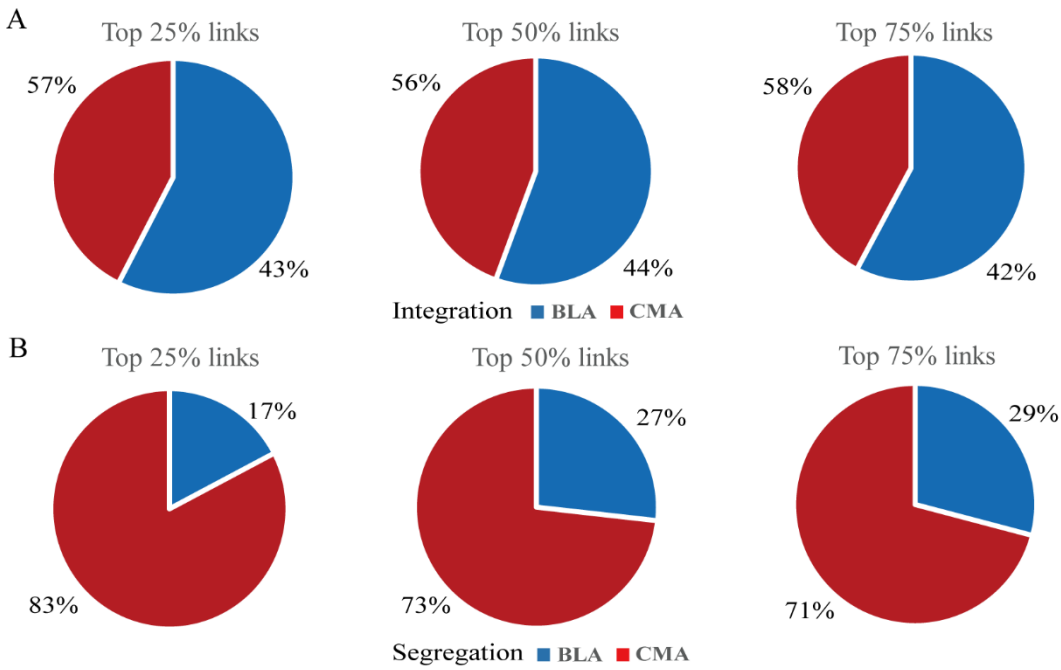

Figure S7. Patterns of relative contribution ratio between BLA and CMA networks in integration and segregation states. Relative ratio of contribution weights between BLA and CMA-target networks are plot in the pie charts, controlled by different inclusion criterion for total links in integration (top) and segregation (bottom) state separately.